Orientation-dependent stress evolution in diamond abrasive grains under directional loading

G. Brune [1], T. Tsagkir Dereli [2], L. Olschewski [1], N. F. Lopes Dias [3], M. Kipp [2], D. Biermann [2] and J. Debus [1,4,*]

[1]*Department of Physics, TU Dortmund University, 44227 Dortmund, Germany*

[2]*Institute of Machining Technology, TU Dortmund University, 44227 Dortmund, Germany*

[3]*Institute of Materials Engineering, TU Dortmund University, 44227 Dortmund, Germany*

[4]*Dortmund Center for Advanced Exploration of Dynamics Across Limits Using Spectroscopy (DAEDALUS), TU Dortmund University, 44227 Dortmund, Germany*

(Received 15 September 2025; accepted 1 April 2026; published 29 April 2026)

Understanding the response of diamond abrasive grains to mechanical loading remains crucial for optimizing their performance in precision manufacturing. In that context, the role of the initial residual stress and crystallographic orientation of the grains is poorly understood. We investigate synthetic diamond grains in two different grit sizes (D126, D252) subjected to directional loading up to 100 N using x-ray diffraction and spatially resolved Raman spectroscopy. Small grains with preferential (111) orientation show an unexpected stress evolution under contact pressures up to 16 GPa, with Raman shifts increasing from 1331.3 to 1333.0 cm^{-1}, indicating an enhanced local compressive stress state at the probed surface regions. Conversely, large (311)-oriented grains exhibit a heterogeneous stress development with Raman shifts varying from 1331.5 to 1332.6 cm^{-1}, including regions that become more tensile (or less compressive) relative to their initial state. The relationship between the relative Raman shift and a spatially weighted contact pressure follows an empirical power law $\delta E \propto p_c'^{\alpha}$ with opposite, orientation-dependent exponents: $\alpha \approx +0.25$ for (111) grains showing progressive compression enhancement and $\alpha \approx -0.35$ for (311) grains exhibiting a trend toward tensile stress components with increasing load. Molecular dynamics simulations reveal that the Schmid factor governs this orientation-dependent response: The low Schmid factor (0.27) for [111] loading restricts dislocation glide, leading to stress retention with high elastic recovery, while the high Schmid factor (0.45) for [311] loading facilitates plastic flow and stress relaxation despite lower peak stress. These findings demonstrate that stress evolution in diamond under directional loading is controlled by the geometric relationship between loading direction and slip systems, providing mechanistic insights for diamond tool design.

DOI: 10.1103/nfgy-gn6j

I. INTRODUCTION

Diamond's exceptional hardness, thermal conductivity, and low friction coefficient make it indispensable for precision grinding applications demanding high surface quality and tight dimensional tolerances [1–3]. However, despite widespread use, the performance of diamond tools remains limited by wear mechanisms that are not fully understood [4,5]. Although thermal degradation pathways such as sp^2 hybridization (graphitization) have been extensively characterized [6–8], the role of mechanical stress in the modification of the diamond lattice during grinding has received comparatively little attention [9]. This gap is significant because individual abrasive grains can experience contact pressures in the multi-GPa range, conditions that may induce permanent structural modifications affecting tool integrity and longevity.

The mechanical response of diamond is governed by pronounced crystallographic anisotropy. Hardness, wear resistance, and fracture behavior vary substantially with crystallographic orientation [5,10]. Diamond anvil cell studies under hydrostatic pressure have established that the Raman-active T_{2g} phonon mode shifts by approximately 2.9–3.2 $cm^{-1}\,GPa^{-1}$ [11–14], providing a well-calibrated stress probe. However, grinding involves highly localized, nonhydrostatic loading along specific crystallographic directions [15], potentially producing mechanical responses distinct from the hydrostatic case [16]. The Raman response itself shows sensitivity to the character of the stress state, with different pressure coefficients observed under nonhydrostatic conditions [17]. How these orientation-dependent responses manifest in real abrasive grains under grinding-relevant loads remains insufficiently understood.

For industrial applications, synthetic diamonds produced by high-pressure high-temperature (HPHT) synthesis dominate the abrasive market because of their consistent quality and controlled impurity levels. The growth process introduces residual stresses whose magnitude and distribution depend on the synthesis conditions [18,19], while subsequent crushing to achieve target grain sizes occurs preferentially along {111} cleavage planes [20,21]. Depending on the size,

*Contact author: joerg.debus@tu-dortmund.de

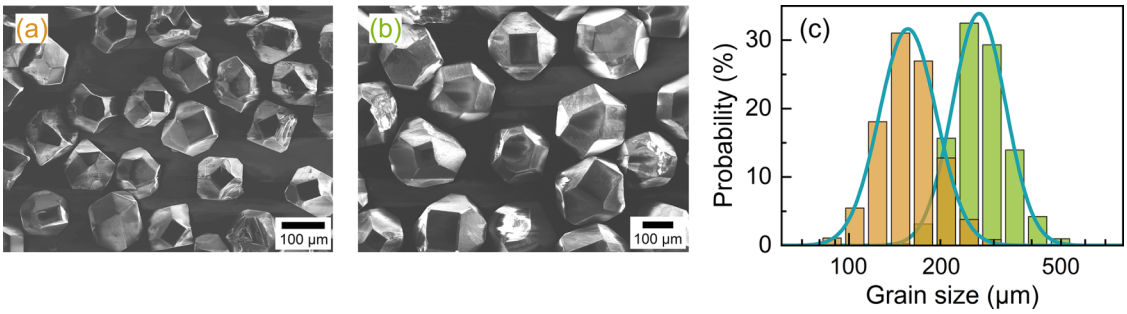

FIG. 1. Scanning-electron-microscopy images of the (a) D126 and (b) D252 diamond grains using 30 kV for the primary electron acceleration and a working distance of 9 and 14 mm, respectively. To determine the surface topography, secondary electrons are detected in scanning mode at a magnification of 50×. (c) Distribution of grain sizes (half-logarithmic presentation) evaluated from batches of both types of diamond grains. The cyan-colored curves present normal distributions.

grains may exhibit different preferred crystallographic orientations that could fundamentally determine how different grain populations respond to mechanical loading. However, the relationship between grain size, crystallographic texture, and stress evolution under load has not been characterized.

The orientation dependence of mechanical properties in diamond, arising from its elastic anisotropy and the geometry of the $\{111\}\langle 110\rangle$ slip systems, is well established from fundamental crystal physics [22]. However, while the qualitative principle is known, quantitative predictions of how this anisotropy manifests in residual stress states after loading cycles in real abrasive grains have been lacking. Recent studies have focused primarily on macroscopic failure modes such as grain fracture and pullout [3,4,23–26], while the question of whether crystallographic orientation can determine not merely the magnitude but the *sign* of residual stress evolution has not been addressed for diamond under grinding-relevant conditions. Furthermore, the counterintuitive possibility that orientations experiencing lower peak stress might exhibit greater plastic deformation due to favorable slip geometry has not been systematically demonstrated. These open questions motivate the central objective of the present work: to determine whether and how crystallographic orientation governs the mechanical stress response of diamond abrasive grains.

In this work, we investigate stress evolution in single HPHT diamond grains of two grit sizes (D126, D252) subjected to controlled directional loading up to 100 N. Combining x-ray diffraction (XRD) texture analysis with spatially resolved confocal Raman spectroscopy, we characterize initial stress states and their modification under contact pressures reaching approximately 16 GPa. We demonstrate that crystallographic orientation critically determines the stress response: (111)-oriented grains exhibit progressive compression enhancement following an empirical power law with positive exponent, while (311)-oriented grains develop heterogeneous stress distributions including regions that become more tensile relative to their initial state. Molecular dynamics (MD) simulations elucidate the underlying mechanism through the Schmid factor, which governs the geometric relationship between applied stress and slip systems. These findings reveal that stress evolution in diamond under directional loading is qualitatively controlled by crystallographic orientation, offering insights for developing more durable abrasive tools through controlled grain selection.

II. MATERIALS AND METHODS

A. Diamond abrasive grains

The single diamond abrasive grains studied are blocky in shape, as shown by scanning-electron-microscopy images in Figs. 1(a) and 1(b). Blocky grains are stable in shape and resistant to wear. The diamond abrasive grains were produced by the HPHT method [27,28]. HPHT diamond abrasive grains are typically single crystals that exhibit different growth faces with varying impurity incorporation. After the growth process, the samples were crushed to achieve specific grain sizes. For our studies, single diamond grains of grit sizes D126 and D252 were used. Based on a random sample (volumetric quantity about 1 cm^3), the distribution of the grain size was measured using a particle analysis device (Micro Trac S3000) based on Mie scattering. The distributions for both grain types are shown in Fig. 1(c). The average grain sizes are determined to $\bar{D}_{\mathrm{small}} = \bar{D}_{\mathrm{s}} = (163.9 \pm 0.1)\,\mu\mathrm{m}$ for D126 and $\bar{D}_{\mathrm{large}} = \bar{D}_{\mathrm{L}} = (279.6 \pm 0.4)\,\mu\mathrm{m}$ for D252.

B. Directional loading tests

In order to realize directional loading tests, an experimental setup was designed and implemented on a five-axis grinding machine (Multigrind CA, Adelbert Haas GmbH). A diamond grain was attached to a steel holder with a two-component epoxy resin adhesive, as shown in Figs. 2(a) and 2(b). The grain holder was joined to a grinding wheel holder that was mounted in the machine spindle, as depicted by the photography in Fig. 2(a). As a counterpart, a flat sample made of 100Cr6 with a hardness of (60 ± 2) HRC was used. It was ground with a vitrified bonded cBN tool and fine-finished using an elastically bonded diamond grinding wheel [29]. It was also applied for the steel workpieces generating a high surface quality to ensure that the grain indentation mark on the workpiece is clearly visible for its detection after the pressure tests. Machine-integrated force measurement sensors and an optical microscope placed inside the machine were used to identify the contact point between grain and workpiece. During a loading test, a diamond grain was loaded with a normal force F_{n} up to 100 N that moved unidirectionally against the counterpart. The resulting normal force was measured by a system that consists of piezoelectric load cells, which are implemented in the machine tool structure. The workpieces

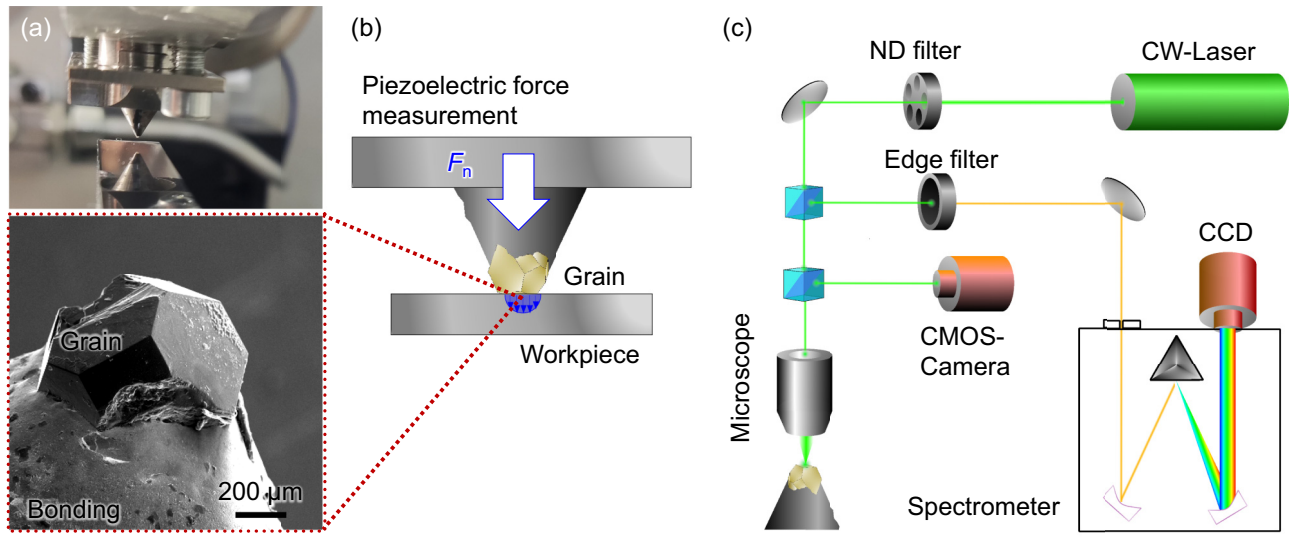

FIG. 2. (a) Photo of a diamond grain inside the five-axis grinding machine including the grain holder and the workpiece below. (b) Scheme of the loading experiments with a magnified view on the grain. (c) Schematic illustration of the Raman scattering setup.

were measured and analyzed by structured illumination microscopy (DUO Vario, confovis GmbH). The indentation area A_c was determined as the contact area, and its change was analyzed as a function of the normal force. The contact area was extracted from the structured illumination microscopy images by identifying the boundary of the indentation mark, which appears as a region of altered surface topography with a clearly defined edge. The area enclosed by this boundary was measured using image analysis software. The nominal contact pressure was calculated by $p_c = F_n/A_c$. Images of single abrasive grains, for determining their geometry, were taken before and after pressure tests using an optical surface measuring device (EdgeMaster, Alicona Imaging GmbH). It was equipped with a 50× magnification lens, which had a numerical aperture of NA = 0.6.

C. Raman scattering spectroscopy

Recent advances in spatially resolved Raman spectroscopy allow for mapping stress fields and structural modifications at the micrometer scale, providing insights into deformation mechanisms in crystalline materials [30–32]. For diamond, the optical phonon mode at about 1332 cm^{-1} serves as a sensitive probe of lattice stress, with both frequency shifts and linewidth changes revealing information about stress states and crystal structure [12,33,34].

Confocal Raman spectroscopy was performed *ex situ* in backscattering geometry using a 532 nm continuous-wave (CW) single-frequency laser (Cobolt Samba, Hübner Photonics); see scheme in Fig. 2(c). The laser power was set to 0.5 mW using neutral density (ND) filters to prevent laser-induced heating of the diamond grains. A microscope objective (LMPLFLN 50×, Olympus) with NA = 0.5 focused the laser light on the grain surface, allowing for a spot diameter of about 0.6 µm. A grain was laterally positioned by a piezo-stage with a reproducible repeatability of < 0.1 µm. Both the laser spot size and the capabilities of the piezo-stage provide Raman imaging with submicrometer resolution. The microscope objective was also used to collimate the light scattered from the grain. Within the detection path, the elastically scattered light was suppressed by an edge filter (LP03-532RE, Semrock). The inelastically Stokes-scattered light was dispersed by a grating with 600 grooves/mm (blazed at 500 nm, silver coated) installed in a monochromator with 0.75 m focal length [35]; the entrance slit width was 25 µm. A charge-coupled-device (CCD) camera (PyLoN:2K, 512 × 2048 pixels, Princeton Instruments) detected the inelastically scattered photons. It yields a spectral resolution of 2.7 cm^{-1} and a point-to-point spectral spacing of 0.85 cm^{-1} allowing for precisely mapping changes in the phonon frequency. The usual acquisition time of a Raman spectrum was 20 s. An optical image of the grain surface was additionally recorded by a monochrome complementary metal-oxide semiconductor (CMOS) camera (Prosilica GE 1650, Allied Vision) to set the points for the Raman mapping.

III. RESULTS AND DISCUSSION

A. Initial state of diamond grains

In Fig. 3(a), the XRD peaks of both types of grains are shown. Despite the appearance of the (111), (220), and (311) Bragg peaks in both diffraction spectra, it becomes obvious that the small diamond grains preferably possess the (111) orientation, while the large grains exhibit the (311) orientation predominantly. Moreover, as depicted in Fig. 3(b), the Bragg peak characteristic for the (111) crystallographic orientation lies at different diffraction angles for both grain types: $2\theta_{111,s} = (44.0 \pm 0.1)^\circ$ and $2\theta_{111,L} = (43.5 \pm 0.1)^\circ$.

These size-dependent preferred orientations likely arise from differences in growth kinetics and facet development that typically occur in HPHT growth [19,36]. The $\bar{D}_s$ (D126) fraction presumably underwent more extensive crushing, promoting cleavage along (111) planes, which is diamond's preferential fracture direction [20,21]. The $\bar{D}_L$ (D252) grains retained their original HPHT growth morphology, which commonly exhibits (311) facets [19].

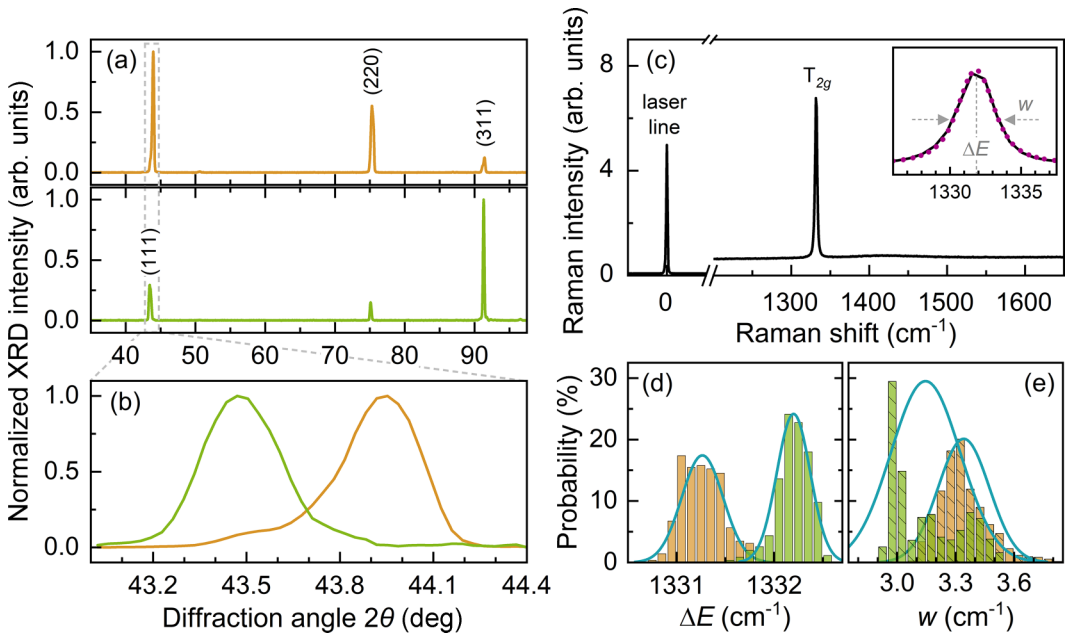

FIG. 3. (a) X-ray diffraction patterns of both types of grains in their initial states; Cu Kα was used as the radiation source. The scanning range is between 30° and 100° and was measured with a step size of 0.035° at a measurement time of 1 s per step. (b) Detailed view on the (111) Bragg peaks. (c) Typical Raman spectrum of a diamond grain; the inset shows the Raman line at about 1331.9 cm^{-1} with high resolution. The magenta-colored curve displays the fitting with a pseudo-Voigt function. Distribution of (d) Raman peak position and (e) linewidth for both grain types in their initial states. The data for the small (large) grains are encoded by the orange (green) color.

The (111) peak shift from about 44.0° to 43.5° represents a lattice expansion in the larger grains along this specific direction. Using Bragg's law $d_{hkl} = \lambda/(2\sin\theta)$ and considering Cu Kα radiation ($\lambda = 1.5406$ Å), one obtains $d_{111,s} \approx 2.056$ Å and $d_{111,L} \approx 2.079$ Å. This indicates different residual stress states along the [111] direction between the two grain types, with the small grains showing compression relative to the large grains. The diffraction angles for the (311) reflection practically coincide with each other, while the (220) reflection shows a 0.15° difference. This observation underlines the anisotropic nature of the residual stress distribution, which is physically reasonable for HPHT diamonds arising from their growth and processing history.

A typical Raman spectrum of a diamond abrasive grain is shown in Fig. 3(c). Apart from the laser line at 0 cm^{-1}, the spectrum predominantly contains the first-order Raman line of the optical phonons [37] at about 1332 cm^{-1}. In addition to that, the background of the spectrum is slightly contributed by the photoluminescence of neutral nitrogen vacancies [38,39]. The Raman peak of diamond is generated by the triply degenerate T_{2g} optical phonon mode at the center (Γ point) of the Brillouin zone. We modeled the Raman line by a pseudo-Voigt function that is contributed by a Gaussian and Lorentzian function [40] and is particularly used to determine the Raman shift ΔE and linewidth. An exemplary fit to the Raman line is depicted in the inset of Fig. 3(c), which demonstrates a pronounced Lorentzian contribution to the fitting curve. The Raman scattering of the grains did not lead to additional peaks that could be ascribed to alternative chemical-structural configurations of the grain surfaces. In the following, the Raman shift and the full width at half maximum (FWHM) are evaluated for $N_s \approx 4500$ and $N_L \approx 2000$ points measured at both grain types. As shown in Fig. 3(d), the Raman shifts exhibit normal distributions with mean values $\overline{\Delta E}_s = (1331.264 \pm 0.003)$ cm^{-1} and $\overline{\Delta E}_L = (1332.199 \pm 0.004)$ cm^{-1}. Thus, the statistical value $t_{\Delta E}$ is given by 187, which demonstrates high statistical significance. As depicted in Fig. 3(e), the full width at half maximum w deviates from a normal distribution for each grain type. Nevertheless, we calculate the mean values $\overline{w}_s = (3.341 \pm 0.002)$ cm^{-1} and $\overline{w}_L = (3.145 \pm 0.004)$ cm^{-1} with a still quite significant $t_w = 44$.

The Raman shift response depends on the stress tensor components and the probed crystallographic orientation through the diamond's elastic and phonon deformation potentials. The anisotropic elastic constants of diamond ($C_{11} = 1076$ GPa, $C_{12} = 125$ GPa, $C_{44} = 577$ GPa) ensure that different crystallographic orientations respond differently to applied stress [41]. The XRD and Raman measurements provide complementary information about the anisotropic stress states in these grains. While XRD probes specific lattice plane spacings, Raman spectroscopy samples the stress state along the direction perpendicular to the dominant grain surface and within a near-surface probe volume. Crucially, for the small grains with preferential (111) surface orientation, the Raman measurement probes the [111] direction, yielding 1331.3 cm^{-1} and thus indicating phonon softening and a more tensile or less compressive stress state along this direction compared to the reference 1332 cm^{-1}. For the large grains with (311) surface orientation, the Raman probes the [311] direction, giving 1332.2 cm^{-1} (indicating a relatively more compressive stress state along this probing direction).

This apparent discrepancy with XRD, which shows [111] compression for small grains, is resolved by recognizing that XRD measures the bulk lattice spacing of (111) planes throughout the grain, while Raman probes the local

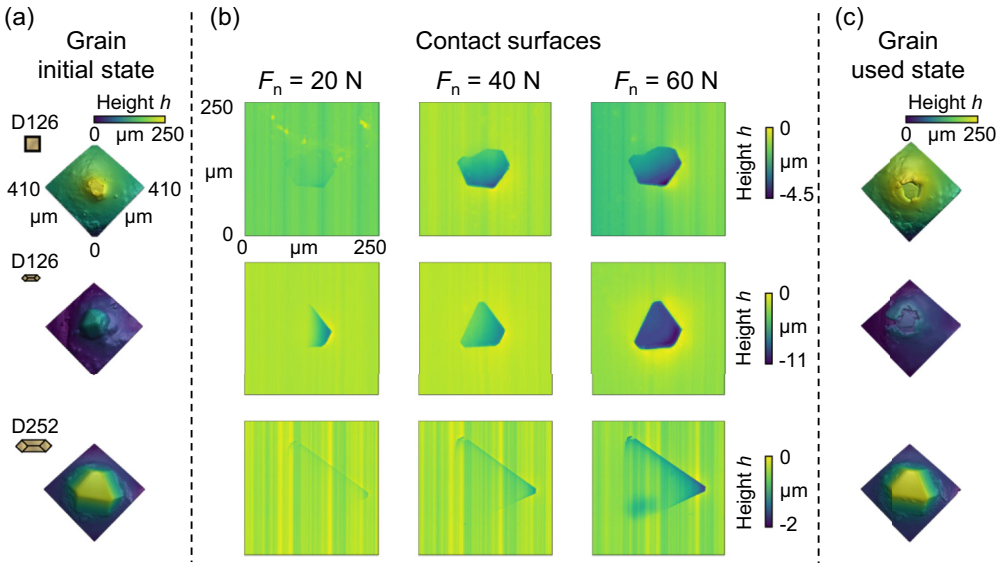

FIG. 4. Microscopic images of the diamond grains in their (a) initial and (c) used states are shown in the left and right columns, respectively. In the middle columns [panel (b)], the contact surfaces observed in the workpieces are illustrated; they were optically recorded after the application of different normal forces to the grains. The first (second) row contains data of the small grain D126 with surface (line)-based contact. The third row is devoted to the large grain D252 with line-based contact.

near-surface stress state along the laser beam direction. The small grains thus exhibit a complex stress state: bulk compression along [111] planes (XRD) but a more relaxed or even tensile stress state at the (111) surface (Raman), likely due to surface relaxation effects and the anisotropic stress field generated during crushing. The difference of about 0.9 cm^{-1} in Raman frequency between the grain types reflects these distinct near-surface stress states arising from their different processing histories.

The widths of the Raman lines provide details about the microstructural state of the grains. The larger linewidth of about 6% for small grains suggests a greater variation in local stress within these grains, presumably due to the crushing process. Since the T_{2g} Raman lines are symmetric and only moderately broadened compared to high-quality synthetic diamond ($w \approx 1.5$–2.0 cm^{-1}) [42], the grains retain single-crystal-like character. They likely contain multiple growth sectors whose internal boundaries contribute to the linewidth. However, characteristic effects of nanocrystallites, such as pronounced asymmetric line broadening due to phonon confinement [33,43,44], are not observed, and there is therefore no Raman evidence for a significant nanocrystalline fraction. The absence of sp^2 hybridized carbon at grain boundaries is also supported, as this would lead to additional broad Raman peaks around 1350 cm^{-1} (D band) and 1580 cm^{-1} (G band) [45,46], which are not detected in our spectra. The nitrogen impurities and vacancies typical for HPHT diamonds may cause additional minor broadening of the T_{2g} Raman line.

B. Directional loading: grain shape and size effects

Due to the heterogeneous grain morphology, the comparability of interactions between a single grain and the hardened steel workpiece is limited. For this reason, only blocky diamond grains with a cubic to octahedral shape were considered in our study. The diamond grains were clustered based on the dominant type of contact with the workpiece, acknowledging that purely idealized forms are not realized due to stochastic influences: (1) predominantly surface-based contact and (2) predominantly line-based contact. Figure 4 shows microscopic images of the grains in their initial (left column) and used state (right column) depending on their cluster type and grain size. The corresponding contact surfaces, i.e., the indentation areas in the hardened steel workpiece, are also depicted for different normal forces F_n.

The contact areas are used to identify the regions of the grains that were subjected to the normal force. This allows for estimating the resulting nominal contact pressures while neglecting reversible effects, such as the elastic deformation of the steel specimen or the deformation of the bond between the abrasive grain and the carrier body. As shown by the microscopic images of the indentations in the workpieces in Fig. 4, in the case of a surface-based contact, only slight indentations are visible, for a low normal force. A full-surface contact is observed for $F_n \geqslant 40$ N. The indentation depth is relatively homogeneous at about 4 µm with a slight gradient toward the bottom-right edge. By comparison, the grains with predominantly line-based contact form narrow indentation areas whose sizes increase with increasing normal force. The indentation depth is significantly high, in particular for the small grain. Starting from the exposed edge of the grain, a gradually decreasing contact pressure distribution along the contact area can be assumed. It is supposed that the local contact pressure p_c is variable due to the varying indentation depth h, and p_c is high in areas with large h. In contrast to that, the large diamond grain D252 shows less pronounced indentation marks and a gradient along the contact edge. This behavior is attributed to a large contact area and a weakly exposed contact edge of the grain.

As shown in Figs. 5(a) and 5(b), for the small grains D126, higher nominal contact pressures are observed at larger normal forces compared to large grains. For the small grain

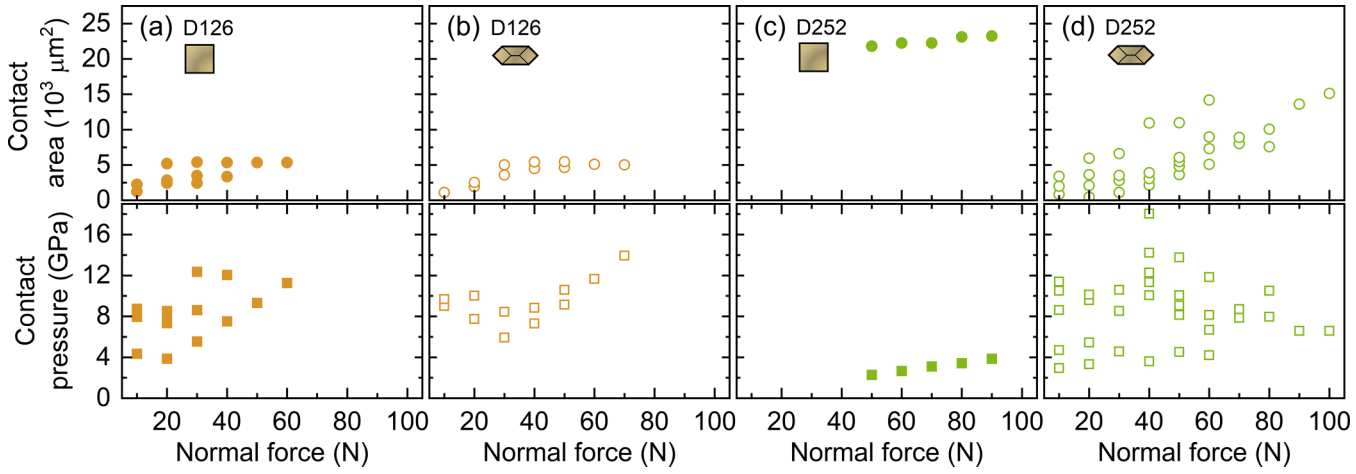

FIG. 5. Influences of grain shapes and sizes on the contact area (top row) and contact pressure (bottom row). Dependencies of A_c and p_c on the normal force F_n are shown for the small grains in (a) surface-based contact and (b) line-based contact. The corresponding dependencies are depicted in panels (c) and (d) for the large grains with surface- and line-based contacts, respectively.

with line-based contact, p_c initially decreases with increasing normal force, similar to the behavior of the grain D252 [see Fig. 5(d)]. However, with $F_n \geqslant 40$ N the contact pressure increases, since the entire grain surface was in contact with the workpiece and no further change in the contact surface occurred. For the large grain, the contact area A_c grows more strongly with increasing F_n in case of the line-based contact in comparison to the surface-based contact shown in Fig. 5(c). This behavior leads to a reduction in the nominal contact pressure. In contrast, the experiments with the predominantly surface-based contact show low p_c due to the large full-surface contact, although it increases with increasing normal force. The contact pressures acting on the grains during the tests did not cause any visible changes in the grain shape (see Fig. 4, right column). The small grains were partially pressed into the bond and carrier body by the high contact pressures acting on them. Due to the partially inhomogeneous indentation depths, it is assumed that the contact pressure is locally variable. Therefore, the indentation depth h is applied as a weighting factor to obtain a spatially resolved, effective contact pressure p_c' in the following Raman analysis.

C. Stress evolution in diamond grains evaluated from Raman imaging

The Raman mappings of the diamond grain surfaces measured after directional loading are shown in Fig. 6. The left column of panels displays the optical images of the contact surfaces, the middle column contains the spatial distributions of the relative Raman shift $\delta E_{s(L)} = \Delta E_{s(L)} - \overline{\Delta E}_{s(L)}$, and the right column presents the spatially resolved effective contact pressures p_c'. To facilitate a point-by-point comparison, the scaling of each contact pressure map was adapted to that of the Raman mapping. The top (middle) row of panels is devoted to the small grains with a surface (line)-based contact. The row of panels at the bottom of Fig. 6 contains the results of the large grain with line-based contact. This presentation directly corresponds to the indentation marks shown in Fig. 4 and allows for evaluating the effect of engagement geometry and grain size on the stress evolution.

As depicted in Fig. 6(b), the small grain D126 with surface-based contact exhibits a gradient in the Raman shift, which is increased significantly in comparison to the initial state: At positions exposed to $p_c' \approx 16$ GPa [see Fig. 6(c)], the Raman shift reaches approximately 1333.0 cm^{-1} ($\delta E_s = 1.7$ cm^{-1}). For areas where p_c' is evaluated to 1.5 GPa, the Raman shift lies at about 1332.2 cm^{-1} ($\delta E_s \approx 1.0$ cm^{-1}). The spatial distributions of the Raman shift and effective contact pressure indicate a direct correlation following $\delta E_s \propto p_c'$; the Raman shift increases systematically with effective contact pressure, indicating a progressive enhancement of compressive stress at the probed surface regions. A similar correlation is observed for the small grain with line-based contact, given in the middle row of panels in Fig. 6. Here, for a variation in p_c' from 10 to 15 GPa [Fig. 6(f)], δE_s goes approximately from 0.1 to 0.6 cm^{-1}. In addition to these gradients, at the darkish spots that are observed sporadically on the surfaces shown in Figs. 6(a) and 6(d), the relative Raman shift exhibits significantly low values [see Figs. 6(b) and 6(e)]. These local changes in the image contrast suggest micrometer-sized dips within the grain surface that could only weakly be illuminated by the white light of the microscope and that experienced lower local stresses.

The observed correlation $\delta E_s \propto p_c'$ indicates that the small grains with (111) orientation undergo a net compression enhancement at the surface regions probed by Raman scattering under loading. This behavior may be attributed to several factors specific to [111] loading: First, the (111) surface represents the closest-packed plane in diamond's cubic structure, offering high resistance to normal compression. When loaded along [111], the geometric relationship between the loading axis and the $\{111\}\langle 110\rangle$ slip systems results in a low Schmid factor, meaning that the resolved shear stress on slip planes remains relatively low even at high applied stress. This unfavorable slip geometry restricts dislocation-mediated stress relaxation, so that the applied compressive stress cannot be efficiently dissipated through plastic flow. The limited plastic deformation creates permanent structural modifications that retain a compressive stress state after unloading. Second, the initial anisotropic stress state of these grains (compressed

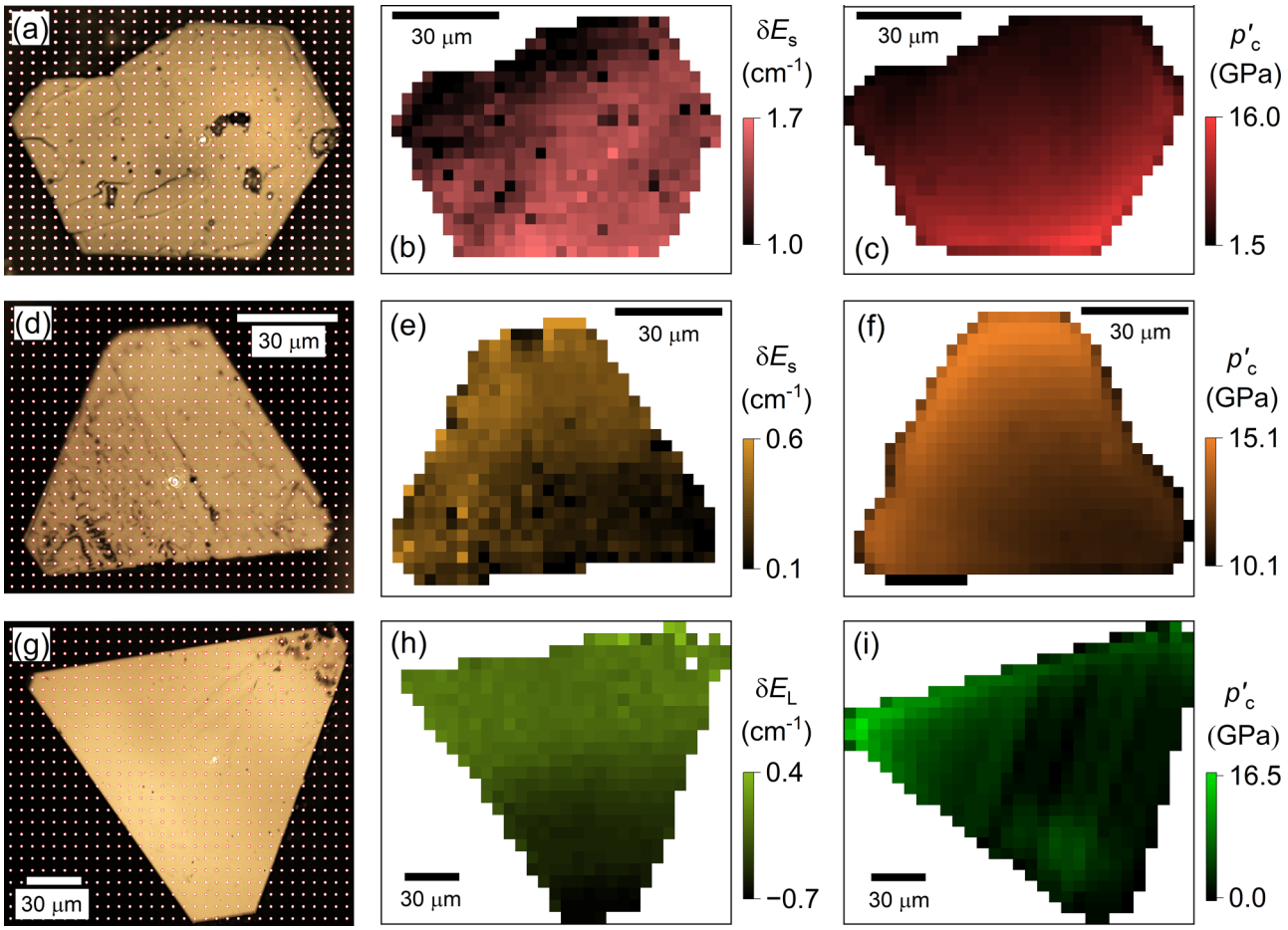

FIG. 6. Optical images and Raman mapping points for a small grain with (a) surface- and (d) line-based contacts and for (g) a large grain with line-based contact, recorded after the loading tests. The mappings contain between 800 and 900 measurement points. Panels (a) and (d) have the same spatial scaling. For the corresponding grains, the middle column [panels (b), (e), and (h)] shows the spatial distribution of the relative Raman shift. The right column [panels (c), (f), and (i)] illustrates the spatial distribution of the effective contact pressure p'_c. It was calculated using $p'_c = (h_p \times F_n)/(h_t \times A_p)$, where h_p is the indentation depth per point, h_t is the total indentation depth, and A_p is the area per point.

in bulk but with partial surface relaxation, as inferred from XRD and Raman data) may undergo stress redistribution under loading. The applied pressure could drive material from subsurface regions toward the surface, effectively "locking in" additional compression at the surface layer probed by Raman spectroscopy. These mechanistic pictures are consistent with the Raman scattering observations and are supported by the molecular dynamics simulations presented in Sec. III D.

For the large grains characterized by a line-based contact, p'_c exhibits a gradient from approximately 0 to 16.5 GPa [see Fig. 6(i)]. Interestingly, for the corresponding spatial positions probed by Raman scattering [Fig. 6(h)], the Raman shift varies from 1331.5 to 1332.6 cm^{-1} (-0.7 $cm^{-1} < \delta E_L < 0.4$ cm^{-1}), with several positions showing $\delta E_L \leqslant 0$. This indicates a heterogeneous stress response with regions whose stress state becomes more tensile (or less compressive) relative to the initial state, even though the global loading is compressive. This behavior, contrasting with that of the small grains, is attributed to loading along the low-symmetry [311] direction. The [311] orientation creates unequal resolved shear stresses on the four {111} slip planes in diamond, leading to nonuniform deformation. The heterogeneous stress state—with both tensile-like and compressive regions observed in the Raman mapping—suggests complex stress redistribution that cannot be accommodated through uniform deformation. The development of regions with reduced Raman shift (more tensile components) alongside compressed regions indicates that the material response involves localized stress concentrations and partial stress relief zones.

Figure 7 compares the relative Raman shifts with the effective contact pressures, for both grit sizes and contact geometries. The data distributions can be described by an empirical power law $\delta E \propto p'^{\alpha}_c$. The exponent takes values of $\alpha \approx +0.25 \pm 0.04$ for the small grains with surface-based contact and $\alpha \approx -0.35 \pm 0.06$ for the large grain with line-based contact. These opposite signs of the power-law exponent represent qualitatively different stress evolution trends. The positive exponent for [111]-oriented grains indicates progressive compression enhancement with increasing effective load, while the negative exponent for [311]-oriented grains reflects the development of more tensile (or less compressive) stress components with increasing effective pressure. The sublinear scaling ($|\alpha| < 0.5$) in both cases suggests a tendency toward saturation at high effective pressures. The contrasting

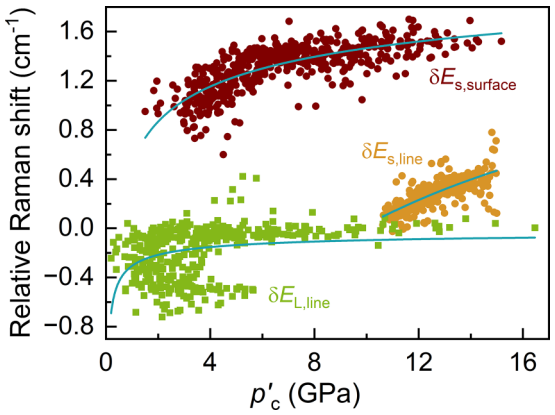

FIG. 7. Relative Raman shift as a function of the spatially resolved effective contact pressure, for the small and large grains shown in Fig. 6. The cyan-colored lines represent fitting curves based on the empirical power law $\delta E \propto p_c'^{\alpha}$.

behaviors demonstrate that stress evolution in diamond grains is not merely a simple elastic response to loading but involves orientation-dependent permanent modifications.

These findings reveal that crystallographic orientation not only influences the magnitude but also strongly influences the direction and character of stress evolution in diamond under directional loading. The opposite signs of the empirical power-law exponents provide a striking illustration of how crystal symmetry dictates mechanical response, with implications for understanding diamond tool performance where grain orientation may determine whether regions experience compression enhancement or a trend toward tensile stress development under otherwise identical loading conditions.

The darkish spots observed in the optical images [Figs. 6(a) and 6(d)], which correspond to reduced δE_s values in the Raman maps [Figs. 6(b) and 6(e)], indicate local variations in the stress state. These features likely represent surface topographical variations (dips or scratches) that were less subjected to the applied load, maintaining stress states closer to the initial condition. The spatial correlation between optical contrast and Raman shift variations highlights the importance of surface topography in determining local stress evolution.

Despite the significant stress modifications observed, the grain integrity is maintained. No structural phase transformations that would reduce crystalline quality are detected, such as transformation from sp^3 to sp^2 carbon hybridization, which would manifest as the D and G Raman bands. Additionally, the spatial distributions of the linewidth w show only slight enhancement at the contact areas [47]. This minimal linewidth change, combined with the absence of peak asymmetry or additional Raman features, demonstrates that the crystalline integrity of the diamond grains is preserved despite the permanent stress modifications. The observed stress evolution thus occurs within the diamond structure without inducing detectable graphitization or amorphization.

It should be noted that the Raman measurements were performed *ex situ*, after the loading-unloading cycle, rather than during active loading. Under uniaxial or deviatoric stress, the triply degenerate T_{2g} mode can in principle split into singlet and doublet components due to symmetry lowering [12,17]. However, in our *ex situ* spectra, no evidence of peak splitting or asymmetry was observed for either grain orientation. The symmetric, single-peak character of all measured Raman lines indicates that the residual stress state after unloading does not induce sufficient symmetry breaking to lift the T_{2g} degeneracy detectably. *In situ* measurements during active loading would be required to characterize the transient stress state under maximum load, where deviatoric components and potential mode splitting may be more pronounced.

D. Molecular Dynamics Simulations

To elucidate the mechanistic origin of the orientation-dependent stress evolution observed experimentally, MD simulations were performed using LAMMPS [48]. Diamond structures containing approximately 30 000 carbon atoms were constructed with a lattice parameter of $a = 3.57$ Å, where the simulation cells were oriented with the compression axis along [111] and [311], respectively, to match the experimental loading configurations. For the [111]-oriented samples, the crystallographic axes were set as $x \parallel [\bar{1}10]$, $y \parallel [11\bar{2}]$, and $z \parallel [111]$, while for the [311]-oriented samples the axes were $x \parallel [01\bar{1}]$, $y \parallel [\bar{2}33]$, and $z \parallel [311]$. To represent the cumulative effect of various defect structures present in HPHT diamond, including vacancies, dislocations, and growth sector boundaries, an effective defect concentration of 2% random vacancies was introduced into the lattice prior to equilibration. The interatomic interactions were described by the Tersoff potential (C.tersoff) [49] parametrized for carbon, which accurately reproduces the elastic properties of diamond including the bulk modulus and the orientation-dependent Young's modulus.

The simulation protocol was designed to mimic the experimental loading-unloading cycle and consisted of five phases, as depicted in Fig. 8(a): equilibration at 300 K and zero pressure (0.1 ns), followed by uniaxial compression along the z axis at a constant engineering strain rate of 2×10^7 s^{-1} while maintaining zero stress in the lateral directions (4 ns), a hold period at maximum strain (2 ns), unloading at the same rate until recovery of the original dimensions (2 ns), and finally relaxation at zero external stress to determine the residual deformation (3 ns). Three strain levels were investigated for [111] diamond (2%, 5%, and 8% compressive strain), while [311] diamond was simulated at 8% strain for direct comparison with the [111] case.

The stress-strain response, shown in Fig. 8(b), reveals pronounced elastic anisotropy between the two orientations. The [111] direction exhibits a Young's modulus of $E_{[111]} = 1280$ GPa, substantially higher than $E_{[311]} = 1080$ GPa for the [311] direction, consistent with [111] being the stiffest crystallographic direction in diamond. At maximum compression of 8% strain, [111] diamond reaches a peak stress of $P_{zz} = 102.4$ GPa, while [311] diamond attains only 86.4 GPa at the same applied strain. The von Mises stress evolution during the complete loading-unloading cycle [Fig. 8(a)] shows that, despite experiencing lower peak stress, the [311] orientation exhibits a larger hysteresis loop upon unloading, suggesting more extensive irreversible deformation.

This counterintuitive observation is quantified by the residual strain simulations summarized in Fig. 8(c). For [111]

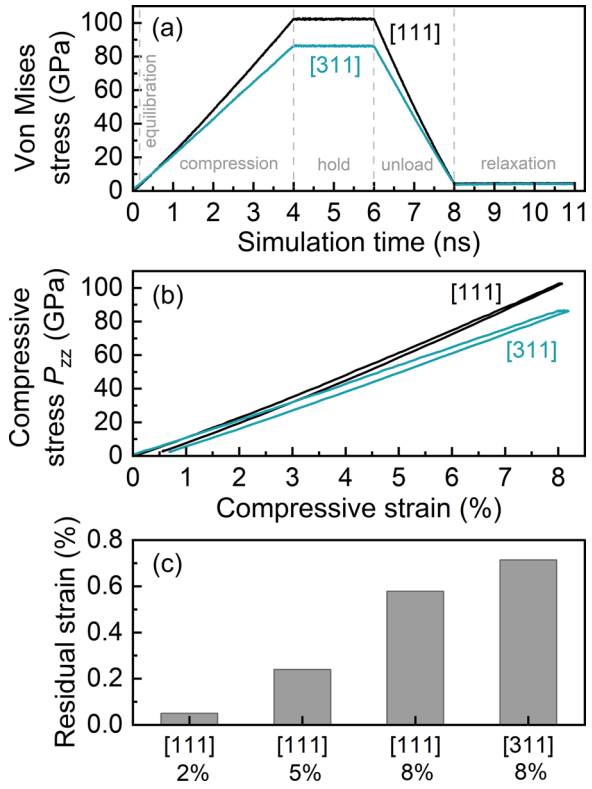

FIG. 8. Molecular dynamics simulation results. (a) von Mises stress evolution during the loading-unloading cycle for [111] and [311] diamond at 8% maximum compressive strain. (b) Compressive stress P_{zz} as a function of compressive strain, showing the stress-strain hysteresis for both orientations. (c) Residual strain after complete unloading for the different simulated cases: [111] diamond at 2%, 5%, and 8% applied strain, and [311] diamond at 8% applied strain.

diamond, the residual strain increases progressively with applied strain: 0.05% at 2% strain (corresponding to about 23 GPa peak stress), 0.24% at 5% strain (about 61 GPa), and 0.58% at 8% strain (102.4 GPa). This corresponds to elastic recovery decreasing from 97.5% to 92.8% as the stress level increases. Critically, despite [111] diamond experiencing substantially higher peak stress, the [311] orientation exhibited 24% larger residual strain (0.714%) than [111] (0.578%) at identical applied strain. This result demonstrates that the magnitude of plastic response is not determined solely by stress level but depends critically on crystallographic orientation.

The orientation-dependent plastic response can be understood through the Schmid factor m, which quantifies the geometric relationship between the applied stress axis and the available slip systems. Diamond deforms plastically via dislocation glide on {111} planes in ⟨110⟩ directions. For [111] loading, the maximum Schmid factor is only 0.27, meaning that the resolved shear stress on slip planes remains relatively low even at high applied stress. In contrast, for [311] loading the Schmid factor reaches 0.45, resulting in significantly higher resolved shear stress for the same applied load. At 8% strain, the resolved shear stress $\tau = P_{zz} \times m$ yields $\tau_{[111]} = 27.6$ GPa for the [111] case, compared to $\tau_{[311]} = 38.9$ GPa for the [311] case. Thus, despite lower applied stress, [311] diamond experiences 41% higher resolved shear stress on its slip systems, which explains its enhanced plastic deformation.

These simulation results provide a mechanistic explanation for the experimentally observed orientation-dependent stress enhancement factors. For [111] grains exhibiting $\alpha = +0.25$, the low Schmid factor restricts dislocation glide, causing the applied compressive stress to be largely retained within the grain even after load removal. The simulations demonstrate that [111] diamond maintains predominantly elastic behavior (greater than 92% recovery) even at high stress levels, and this stress retention manifests experimentally as positive Raman shifts corresponding to residual compressive stress. For [311] grains exhibiting $\alpha = -0.35$, the favorable slip geometry enables stress relaxation through plastic flow. Although the peak stress remains lower than for [111], the high Schmid factor facilitates dislocation activity, allowing for partial relaxation of the applied load and resulting in reduced or negative residual stress after unloading. The larger residual strain in [311] diamond reflects stress accommodation through plastic flow, whereas the smaller residual strain in [111] diamond indicates that applied stress is retained as elastic strain energy rather than being dissipated through dislocation motion.

While the MD simulations employ significantly higher stresses than the nominal experimental contact pressure, they capture the essential physics governing orientation-dependent mechanical response. The actual contact between a flat countersurface and an irregularly shaped grain produces highly inhomogeneous stress distributions, with local stresses at edges and asperities, substantially exceeding the nominal value. These local stress concentrations can surpass the critical shear stress for athermal dislocation nucleation, allowing for permanent structural modifications without requiring thermal activation. Furthermore, the *relative* plastic response between orientations is governed by geometric factors (the Schmid factor) that remain valid across stress regimes. The opposing trend between Schmid factor and experimental α confirms that crystallographic orientations with higher Schmid factors, and thus easier slip activation, exhibit lower or negative stress enhancement factors due to stress relaxation through plastic deformation.

IV. CONCLUSION

This study establishes that stress evolution in diamond abrasive grains under directional loading is governed by the crystallographic relationship between loading direction and slip systems, which can be quantified through the Schmid factor. The key finding is that (111)-oriented grains exhibit progressive compression enhancement ($\alpha \approx +0.25$) due to restricted dislocation glide associated with a low Schmid factor of 0.27, while (311)-oriented grains develop heterogeneous stress distributions including regions with tensile components ($\alpha \approx -0.35$) through favorable plastic flow geometry enabled by a high Schmid factor of 0.45. Molecular dynamics simulations confirm this mechanistic picture: Despite [111] diamond experiencing higher peak stress (102.4 GPa compared to 86.4 GPa for [311]), the [311] orientation exhibits 24% larger residual strain owing to its 41% higher

resolved shear stress on the active slip systems. These results reveal that even diamond undergoes significant orientation-dependent plastic deformation at grinding-relevant pressures, with outcomes critically determined by crystallographic constraints rather than by the magnitude of applied stress alone. The ability to predict stress evolution through Schmid factor analysis provides a materials physics basis for optimizing diamond tool performance through controlled grain orientation selection, offering a path toward more durable abrasive tools.

ACKNOWLEDGMENT

The authors acknowledge financial support from the German Research Foundation (DFG) under the Project No. 501935718.

DATA AVAILABILITY

The data that support the findings of this article are openly available [50].

[1] E. Brinksmeier, Y. Multlugünes, F. Klocke, J. Aurich, P. Shore, and H. Ohmori, Ultra-precision grinding, CIRP Ann. Manuf. Technol. **59**, 652 (2010).

[2] P. Krajnik, F. Hashimoto, B. Karpuschewski, E. da Silva, and D. Axinte, Grinding and fine finishing of future automotive powertrain components, CIRP Ann. Manuf. Technol. **70**, 589 (2021).

[3] R. Komanduri and M. Shaw, Wear of synthetic diamond when grinding ferrous metals, Nature (London) **255**, 211 (1975).

[4] S. Shimada, H. Tanaka, M. Higuchi, T. Yamaguchi, S. Honda, and K. Obata, Thermo-chemical wear mechanism of diamond tool in machining of ferrous metals, CIRP Ann. **53**, 57 (2004).

[5] L. Pastewka, S. Moser, P. Gumbsch, and M. Moseler, Anisotropic mechanical amorphization drives wear in diamond, Nat. Mater. **10**, 34 (2011).

[6] Q. Bai, Z. Wang, Y. Guo, J. Chen, and Y. Shang, Graphitization behavior of single crystal diamond for the application in nanometric cutting, Curr. Nanosci. **14**, 377 (2018).

[7] V. Howes, The graphitization of diamond, Proc. Phys. Soc. **80**, 648 (1962).

[8] R. Khmelnitsky and A. Gippius, Transformation of diamond to graphite under heat treatment at low pressure, Phase Transitions **87**, 175 (2014).

[9] H. Chacham and L. Kleinman, Instabilities in diamond under high shear stress, Phys. Rev. Lett. **85**, 4904 (2000).

[10] V. Blank, M. Popov, G. Pivovarov, N. Lvova, and S. Terentev, Mechanical properties of different types of diamond, Diam. Relat. Mater. **8**, 1531 (1999).

[11] H. Boppart, J. van Straaten, and I. F. Silvera, Raman spectra of diamond at high pressures, Phys. Rev. B **32**, 1423 (1985).

[12] M. Grimsditch, E. Anastassakis, and M. Cardona, Effect of uniaxial stress on the zone-center optical phonon of diamond, Phys. Rev. B **18**, 901 (1978).

[13] S. S. Mitra, O. Brafman, W. B. Daniels, and R. K. Crawford, Pressure-induced phonon frequency shifts measured by Raman scattering, Phys. Rev. **186**, 942 (1969).

[14] E. Whalley, A. Lavergne, and P. T. T. Wong, Hydrostatic optical cell with glass windows for 25 kilobar, Rev. Sci. Instrum. **47**, 845 (1976).

[15] F. van Bouwelen and W. van Enckevort, A simple model to describe the anisotropy of diamond polishing, Diam. Relat. Mater. **8**, 840 (1999).

[16] H. N. Li, T. B. Yu, L. D. Zhu, and W. S. Wang, Analytical modeling of grinding-induced subsurface damage in monocrystalline silicon, Mater. Des. **130**, 250 (2017).

[17] H. Mohrbacher, K. Van Acker, B. Blanpain, P. Van Houtte, and J.-P. Celis, Comparative measurement of residual stress in diamond coatings by low-incident-beam-angle-diffraction and micro-Raman spectroscopy, J. Mater. Res. **11**, 1776 (1996).

[18] N. I. Alekseyev, A. P. Broyko, I. K. Khmelnitskiy, A. V. Kolyadin, V. M. Aivazyan, and I. V. Oreshko, Temperature- and pressure-reducing regimes in the growth cell of HPHT diamonds, optimal for preserving crystal integrity after growth completion, J. Carbon Res. **9**, 52 (2023).

[19] R. C. Burns, A. I. Chumakov, S. H. Connell, D. Dube, H. P. Godfried, J. O. Hansen, J. Härtwig, J. Hoszowska, F. Masiello, L. Mkhonza, M. Rebak, A. Rommevaux, R. Setshedi, and P. Van Vaerenbergh, HPHT growth and x-ray characterization of high-quality type IIa diamond, J. Phys.: Condens. Matter **21**, 364224 (2009).

[20] R. H. Telling, C. J. Pickard, M. C. Payne, and J. E. Field, Theoretical strength and cleavage of diamond, Phys. Rev. Lett. **84**, 5160 (2000).

[21] S. Ramaseshan, The cleavage properties of diamond, Proc. Indian Acad. Sci. **24**, 114 (1946).

[22] S. G. Roberts, P. D. Warren, and P. B. Hirsch, Hardness anisotropies: A new approach, Mater. Sci. Eng. A **105-106**, 19 (1988).

[23] Q. Wan, L. Zou, S. Liu, T. Wang, S. Chen, and Y. Huang, Investigation on abrasive wear mechanism of single diamond grain in flexible scribing titanium alloy, Diam. Relat. Mater. **120**, 108631 (2021).

[24] C. Dai, W. Ding, J. Xu, Y. Fu, and T. Yu, Influence of grain wear on material removal behavior during grinding nickel-based superalloy with a single diamond grain, Int. J. Mach. Tools Manuf. **113**, 49 (2017).

[25] W. Li, X. Hu, G. Long, A. Shang, and B. Guo, Grain wear properties and grinding performance of porous diamond grinding wheels, Wear **530-531**, 204993 (2023).

[26] S. Buhl, C. Leinenbach, R. Spolenak, and K. Wegener, Failure mechanisms and cutting characteristics of brazed single diamond grains, Int. J. Adv. Manuf. Technol. **66**, 775 (2013).

[27] J. Angus, Diamond synthesis by chemical vapor deposition: The early years, Diam. Relat. Mater. **49**, 77 (2014).

[28] T. Schuelke and T. Grotjohn, Diamond polishing, Diam. Relat. Mater. **32**, 17 (2013).

[29] P. Mativenga, J. Schoop, I. Jawahir, D. Biermann, M. Kipp, Z. Kilic, T. Özel, and R. Wertheim, Engineered design of cutting tool material, geometry, and coating for optimal performance and customized applications: A review, CIRP J. Manuf. Sci. Technol. **52**, 212 (2024).

[30] C. R. Das, H. C. Hsu, S. Dhara, A. K. Bhaduri, B. Raj, L. C. Chen, K. H. Chen, S. K. Albert, A. Ray, and Y. Tzeng, A complete Raman mapping of phase transitions in Si under indentation, J. Raman Spectrosc. **41**, 334 (2010).

[31] F. Bianco, K. Fedus, F. Enrichi, R. Pierobon, M. Cazanelli, M. Ghulinyan, G. Pucker, and L. Pavesi, Two-dimensional micro-Raman mapping of stress and strain distributions in strained silicon waveguides, Semicond. Sci. Technol. **27**, 085009 (2012).

[32] T. Wermelinger, C. Borgia, C. Solenthaler, and R. Spolenak, 3-D Raman spectroscopy measurements of the symmetry of residual stress fields in plastically deformed sapphire crystals, Acta Mater. **55**, 4657 (2007).

[33] J. W. Ager, D. K. Veirs, and G. M. Rosenblatt, Spatially resolved Raman studies of diamond films grown by chemical vapor deposition, Phys. Rev. B **43**, 6491 (1991).

[34] C. Pickard, T. Davis, W. Wang, and J. Steeds, Mapping crystalline quality in diamond films by micro-Raman spectroscopy, Diam. Relat. Mater. **7**, 238 (1998).

[35] H. Moldenhauer, M. Bayer, J. Debus, A. Nikolov, and A. Brümmer, Raman scattering study of micrometer-sized spots of magnetite and hematite formed at 18CrNiMo7-6 screw rotor surfaces due to liquid-free, unsynchronized operation, IOP Conf. Ser.: Mater. Sci. Eng. **425**, 012016 (2018).

[36] S. S. Dossa, I. Ponomarev, B. N. Feigelson, M. Hainke, C. Kranert, J. Friedrich, and J. J. Derby, Analysis of the high-pressure high-temperature (HPHT) growth of single crystal diamond, J. Cryst. Growth **609**, 127150 (2023).

[37] R. Krishnan, Raman spectrum of diamond, Nature (London) **155**, 171 (1945).

[38] D. Braukmann, V. P. Popov, E. R. Glaser, T. A. Kennedy, M. Bayer, and J. Debus, Anisotropies in the linear polarization of vacancy photoluminescence in diamond induced by crystal rotations and strong magnetic fields, Phys. Rev. B **97**, 125426 (2018).

[39] D. Braukmann, E. R. Glaser, T. A. Kennedy, M. Bayer, and J. Debus, Circularly polarized zero-phonon transitions of vacancies in diamond at high magnetic fields, Phys. Rev. B **97**, 195448 (2018).

[40] C. Thomann, A. Wittrock, A. Wittig, N. Dias, D. Stangier, W. Tillmann, and J. Debus, Tuning of solid-to-solid structural transitions in amorphous carbon films by optical pumping and chemical modification, APL Mater. **11**, 031106 (2023).

[41] M. H. Grimsditch and A. K. Ramdas, Brillouin scattering in diamond, Phys. Rev. B **11**, 3139 (1975).

[42] W. Borer, S. Mitra, and K. Namjoshi, Line shape and temperature dependence of the first order Raman spectrum of diamond, Solid State Commun. **9**, 1377 (1971).

[43] A. K. Arora, T. Ravindran, G. Reddy, A. K. Sikder, and D. Misra, Nature of confinement of phonons in nanocrystalline CVD diamond, Diam. Relat. Mater. **10**, 1477 (2001).

[44] S. Osswald, V. N. Mochalin, M. Havel, G. Yushin, and Y. Gogotsi, Phonon confinement effects in the Raman spectrum of nanodiamond, Phys. Rev. B **80**, 075419 (2009).

[45] A. C. Ferrari and J. Robertson, Interpretation of Raman spectra of disordered and amorphous carbon, Phys. Rev. B **61**, 14095 (2000).

[46] J. Robertson, Amorphous carbon, Adv. Phys. **35**, 317 (1986).

[47] See Supplemental Material at http://link.aps.org/supplemental/10.1103/nfgy-gn6j for the FWHM maps and contact pressure distributions.

[48] A. P. Thompson, H. M. Aktulga, R. Berger, D. S. Bolintineanu, W. M. Brown, P. S. Crozier, P. J. in 't Veld, A. Kohlmeyer, S. G. Moore, T. D. Nguyen, R. Shan, M. J. Stevens, J. Tranchida, C. Trott, and S. J. Plimpton, LAMMPS—A flexible simulation tool for particle-based materials modeling at the atomic, meso, and continuum scales, Comput. Phys. Commun. **271**, 108171 (2022).

[49] J. Tersoff, Modeling solid-state chemistry: Interatomic potentials for multicomponent systems, Phys. Rev. B **39**, 5566 (1989).

[50] J. Debus, Orientation-dependent stress evolution in diamond abrasive grains under directional loading, Zenodo (2026), https://doi.org/10.5281/zenodo.18481366.